

P81

**VIRTUAL NEAR-RADAR DOPPLER VELOCITY SIGNATURES OF
LOW-LEVEL SUPERCCELL HORIZONTAL AND VERTICAL ROTATIONS:
SIMULATION STUDY**

Vincent T. Wood³, Robert P. Davies-Jones^{1,3}, and Corey K. Potvin^{2,3,4}
¹Emeritus, ²Cooperative Institute for Mesoscale Meteorological Studies,
³NOAA/OAR/National Severe Storms Laboratory, and
⁴School of Meteorology, University of Oklahoma,
Norman, Oklahoma, USA

1. INTRODUCTION

A large number of studies within the severe storms community have demonstrated that the upward tilting of intense low-level horizontal baroclinically-generated vorticity is a primary source of low-level vertical vorticity in supercell mesocyclones (Rotunno and Klemp 1985; Davies-Jones and Brooks 1993; Brooks et al. 1994; Wicker and Wilhelmson 1995; Trapp and Fiedler 1995; Adlerman et al. 1999 among others). The objectives of the present study are to assess the potential utility of Doppler radar to (a) investigating this vorticity tilting process, and (b) anticipating imminent tornadogenesis. We first developed formulas for the Doppler velocity and vorticity components of radar targets defined in a right-handed radar coordinate system that accounts for earth curvature and beam refraction. Then, we generated radar pseudo-observations of a supercell simulated using the Advanced Research Weather Research and Forecasting (WRF-ARW) model (Skamarock et al. 2008). A tornado developed ~110 min into the simulation and became very intense with surface winds briefly exceeding 110 m s⁻¹ (EF5). Next, we computed Doppler azimuthal and normal vorticity components and assessed their suitability as proxies for the simulated low-level horizontal and vertical vorticity components, respectively. Finally, we related temporal trends in each vorticity component to the simulated tornadogenesis.

2. VORTICITY COMPONENTS IN RADAR COORDINATES

Since a Doppler radar typically measures the along-beam motion of targets within successive azimuthal scans, it is expeditious and computationally economical to determine the observed parts of kinematic quantities from radar data (Davies-Jones and Wood 2019). The structure and steadiness of radar-observed supercell

thunderstorms were examined in terms of the horizontal and vertical components of vorticity. To assess the potential utility of Doppler radar to estimating these vorticity components and thereby exploring the tilting of baroclinically-generated vorticity, we define a right-handed curvilinear coordinate system (r, α, β) centered on the radar, where r is the slant range (arclength along a stationary beam), α is the launch angle (i.e., beam elevation angle at the radar), and β is the azimuth angle measured clockwise from due north. Davies-Jones and Wood (2019) showed that the observable (*ob*) parts of the 3D vorticity vector $\boldsymbol{\omega} = \nabla \times \mathbf{V}$ of the \mathbf{V} -field in curvilinear, radar coordinates are given by

$$(\omega_\alpha)_{ob} = \frac{\kappa_f}{2} \operatorname{cosec}\left(\frac{\kappa_f r}{2}\right) \sec\left(\alpha - \frac{\kappa_f r}{2}\right) \frac{\partial V_r}{\partial \beta} . \quad (2.1)$$

$$(\omega_\beta)_{ob} \approx -\frac{\kappa_f}{\sin(\kappa_f r)} \frac{\partial V_r}{\partial \alpha} . \quad (2.2)$$

In Eqs. (2.1) and (2.2), the radial component of target motion V_r is the observed Doppler velocity component; the other vertical and azimuthal components (Fig. 1) are, respectively, V_α and V_β and unobservable (not shown). Here, Eq. (2.1) represents the so-called ‘‘Doppler normal vorticity’’ and is the observable component of vorticity normal to the surface of a constant launch angle α . The term $\kappa_f = \left(\frac{1}{5.76} - 1\right) \cos \alpha / a$ is the ray curvature for flat-earth geometry developed by Davies-Jones et al. (2019). Here, a is the earth’s radius of 6371 km (Doviak and Zrnić (1993).

Eq. (2.2) is the so-called ‘‘Doppler azimuthal vorticity’’ which is the observable azimuthal vorticity component lying in the azimuthal β direction (Fig. 1). The equation is computed from data collected during two successive elevation scans. The $(\omega_\beta)_{ob}$ signature may be a critical factor in estimating horizontal vorticity near developing mesocyclones and tornadoes, provided that the horizontal rotation axis is perpendicular to the radar viewing direction (Fig. 1). Otherwise, if the rotation axis is parallel to the viewing direction, then the horizontal vorticity is not sampled.

Corresponding Author Address: Vincent T. Wood, National Severe Storms Laboratory, 120 David L. Boren Blvd. Norman, Oklahoma 73072-7323, USA; E-Mail: Vincent.Wood@noaa.gov

In this study, the simulated supercell flow is over a flat earth (with zero earth curvature) instead of a curved one. To maintain the same beam-height function of r and α for different earth curvatures, we need to keep the same earth-surface curvature minus ray curvature. The minus sign in κ_f signifies that the ray curvature relative to a flat earth is concave upwards (Xu and Wei 2013).

3. HIGH-RESOLUTION NUMERICAL MODEL

A “truth” tornadic supercell simulation was generated using version 3.6.1 of the Advanced Research Weather Research and Forecasting (WRF-ARW) model (Skamarock et al. 2008) with 111-m horizontal grid spacing and typical cloud model settings. The 111-m grid was run concurrently within a 333-m simulation in a one-way nested configuration. The 333-m simulation was initialized using a thermal bubble and the Rapid Update Cycle (RUC; Benjamin et al. 2004) sounding valid near the 24 May 2011 El Reno, Oklahoma tornadic supercell (Potvin and Flora 2015). The hodograph in Fig. 2 was used in the El Reno simulation; the storm-relative environmental helicity value of $572 \text{ m}^2 \text{ s}^{-2}$ (Davies-Jones et al. 1990) was calculated. The tornado was rated (enhanced Fujita) EF-5. The evolution of the 333-m supercell simulation was described in Potvin et al. (2017). The nested 111-m simulation was initialized 30 min into the 333-m simulation, at which time a mature supercell was presented. The simulation was integrated for 150 min. The 333-m and 111-m grids used time steps of 1 s and 1/3 s, respectively, with a 50-level stretched vertical grid with spacing increasing from ~ 100 m near the surface to ~ 600 m between 10 km and 22 km AGL (model top). The Thompson microphysics scheme (Thompson et al. 2004, 2008), which includes five hydrometeor categories and predicts two moments of the rain and cloud ice particle size distributions, was used. Turbulence was parameterized using the 1.5-order turbulence kinetic energy (TKE) closure. Radiation was neglected for simplicity. A free-slip lower boundary condition was used, effectively disregarding the effects of surface drag. The lateral boundaries of the 333-m (parent) grid were open; the lateral boundaries of the 111-m nested grid were interpolated from the 333-m grid at each model time step. A Rayleigh damping layer was used at the model top to mitigate reflection of gravity waves off the model top.

4. SIMULATION RESULTS

In this section, we determine whether or not the observable azimuthal vorticity component signature in Eq. (2.2) is a useful tool to help forecasters and/or radar meteorologists anticipate impending tornadogenesis. We first begin our discussion by presenting the evolution of

a supercell that produced a hook echo in association with two tornado-like vortices (hereafter, “tornadoes”) in Fig. 3. A well-pronounced hook echo in association with a low-level intensifying updraft occurred as the first tornado developed ~ 80 min into the simulation (Figs. 4 and 5). The tornado became very intense with surface winds (not shown) briefly exceeding 110 m s^{-1} and a strong updraft surpassing 80 m s^{-1} at low altitudes.

Figure 4 shows several cycles of maximum vertical velocity, suggesting pulsating updrafts near storm top and near ground at different times. The updraft pulsations aloft are not reflected at low altitudes. There are approximately seven low-level updraft maxima below the 2-km height at $t = 71, 91, 113, 125, 131, 140$ and 147 min, whereas numerous upper-level updraft maxima occur around the 10-km height. At low altitudes, updraft intensification and pulsation are closely associated with low-level vertical vorticity intensification and pulsation (Fig. 5), as discussed by Wicker and Wilhelmson (1995). Furthermore, Wicker and Wilhelmson described how vertical vorticity in the mesocyclone and the tornado vortex at low altitudes is initially created by the tilting of the environmental vorticity and baroclinically generated vorticity along the forward flank gust front of the storm.

To evaluate the potential effectiveness of Doppler radar to exploring this process, Figs. 6-9 show the plots of (a) radar reflectivity with superimposed storm-relative horizontal wind vectors, (b) Doppler velocity field corresponding to the wind vectors shown in panel a of the figures, (c) horizontal vorticity vectors and contours, (d) Doppler azimuthal vorticity vectors and contours, (e) vertical vorticity, and (f) Doppler normal vorticity at $t = 60, 70, 80$ and 90 min. The grid size in the figures is $8 \text{ km} \times 8 \text{ km}$, which has been enlarged from the small white square shown in Fig. 3.

Since the Doppler radar senses only the component of flow in the radar viewing direction, zero Doppler velocity (gray band) indicates flow that is entirely perpendicular to the viewing direction (Figs. 6b-9b). The red (green) area represents outbound (inbound) velocities relative to the radar. These Doppler velocity fields correspond to storm-relative, horizontal wind vectors at low levels (Figs. 6a-9a). The Doppler velocity signature fields indicate a transition from strong convergence (Fig. 6b) to strong cyclonic rotation embedded in the convergence region (Fig. 9b). Inspection of the simulation reveals that this is associated with strong inflow spiraling cyclonically toward the center of the updraft base before turning up within the updraft. This is a prominent feature of the organizing stage of a supercell.

The evolving low-level Doppler azimuthal vorticity $(\omega_\beta)_{ob}$ signatures with superimposed vectors from $t = 60$ min through $t = 90$ min are portrayed in panel d of Figs. 6-9, along with the corresponding simulated horizontal

vorticity (ω_H) fields (panel c of the figures). The $(\omega_\beta)_{ob}$ vectors are always perpendicular to the Doppler velocity component (Fig. 1). When the vectors point to the left, $(\omega_\beta)_{ob} < 0$, which indicates negative vertical Doppler velocity shear in the azimuthal direction. Vectors pointing to the right imply positive vertical Doppler shear. Examination of Figs. 6-9 suggests that the $(\omega_\beta)_{ob}$ field (Figs. 6d-9d) is a good proxy for horizontal vorticity ω_H (Figs. 6c-9c), and that the $(\omega_\alpha)_{ob}$ region (Figs. 6f-9f) is a good proxy for vertical vorticity ζ (Figs. 6e-9e). Most importantly, both the $(\omega_\beta)_{ob}$ and ω_H amplify *prior* to the amplification of $(\omega_\alpha)_{ob}$ and ζ . Consequently, we theorize that the evolution of $(\omega_\beta)_{ob}$ signatures may be useful for anticipating imminent tornadogenesis.

Part of the $(\omega_\beta)_{ob}$ signatures lie within very low-reflectivity regions (outside of the purple 0.1-dBZ contour in Figs. 6-9) and may therefore not be detected with real radar. Because beam height increases with slant range, near-surface horizontal vorticity is detectable only at close ranges. The impacts of these observational limitations will be explored in future work.

5. CONCLUSIONS AND FUTURE WORK

A “truth” tornadic supercell simulation was generated using the high-resolution WRF-ARW model. The simulation was conducted to assess estimates of Doppler normal and azimuthal vorticity components diagnosed from virtual near-radar Doppler velocity signatures at low altitudes. Trends in the Doppler azimuthal (normal) vorticity component correspond well to trends in the horizontal (vertical) vorticity component. Amplification of the Doppler azimuthal vorticity signatures at low levels *preceded* the amplification of vertical vorticity. This suggests that these Doppler vorticity signatures may help the radar meteorologists or forecasters anticipate imminent tornadogenesis.

We will continue this work by obtaining real radar data of tornadoes at close proximity to a WSR-88D. The emerging conclusions will determine whether or not the Doppler radar detection of amplifying horizontal vorticity at low levels in supercells could provide early warning of tornadogenesis. If so, this would motivate the development of automated Doppler-based algorithms to provide additional diagnostic information for convective storm nowcasting.

Acknowledgments. The authors thank Terry Schuur of NSSL for providing his helpful comments. Funding was partly provided by NOAA/Office of Oceanic and Atmospheric Research under NOAA-University of Oklahoma

Cooperative Agreement #NA11OAR4320072, U.S. Department of Commerce.

6. REFERENCES

- Adlerman, E. J., K. K. Droegemeier, and R. Davies-Jones, 1999: A numerical simulation of cyclic mesocyclogenesis. *J. Atmos. Sci.*, **56**, 2045–2069, [https://doi.org/10.1175/1520-0469\(1999\)056%3C2045:ANSOCM%3E2.0.CO;2](https://doi.org/10.1175/1520-0469(1999)056%3C2045:ANSOCM%3E2.0.CO;2).
- Benjamin, S. G., and Coauthors, 2004: An hourly assimilation–forecast cycle: The RUC. *Mon. Wea. Rev.*, **132**, 495–518, [https://doi.org/10.1175/1520-0493\(2004\)132%3C0495:AHACTR%3E2.0.CO;2](https://doi.org/10.1175/1520-0493(2004)132%3C0495:AHACTR%3E2.0.CO;2).
- Brooks, H. B., C. A. Doswell III, and R. B. Wilhelmson, 1994: The role of midtropospheric winds in the evolution and maintenance of low-level mesocyclones. *Mon. Wea. Rev.*, **122**, 126–136, [https://doi.org/10.1175/1520-0493\(1994\)122<0126:TROMWI>2.0.CO;2](https://doi.org/10.1175/1520-0493(1994)122<0126:TROMWI>2.0.CO;2).
- Davies-Jones, R., 1984: Streamwise vorticity: The origin of updraft rotation in supercell storms. *J. Atmos. Sci.*, **41**, 2991–3006, [https://doi.org/10.1175/1520-0469\(1984\)041<2991:SVTOOU>2.0.CO;2](https://doi.org/10.1175/1520-0469(1984)041<2991:SVTOOU>2.0.CO;2).
- Davies-Jones, R., and H. Brooks, 1993: Mesocyclogenesis from a theoretical perspective. *The tornado: Its Structure, Dynamics, Prediction, and Hazards, Geophys. Monogr.*, No. 79. Amer. Geophys. Union, 105–114.
- Davies-Jones, R., and V. T. Wood, 2019: Intrinsic coordinates for the WSR-88D system. (Prepared for *MWR*).
- Davies-Jones, R. P., D. W. Burgess, and M. P. Foster, 1990: Test of helicity as a forecast parameter. Preprints, *16th Conf. on Severe Local Storms*, Kananaskis Park, AB, Canada, Amer. Meteor. Soc., 588–592.
- Davies-Jones, R., V. T. Wood, and M. A. Askelson, 2019: Ray curvature on a flat earth for computing virtual WSR-88D signatures of simulated supercell storms. (Prepared for *MWR*).
- Doviak, R. J., and D. S. Zrić, 1993: *Doppler Radar and Weather Observations*. 2nd ed. Academic Press, 562 pp.
- Hildebrand, F. B., 1962: *Advanced Calculus for Applications*. Prentice-Hall, 646 pp.
- Potvin, C. K. and M. L. Flora, 2015: Sensitivity of idealized supercell simulations to horizontal grid spacing: Implications for Warn-on Forecast. *Mon. Wea. Rev.*, **143**, 2998–3024, <https://doi.org/10.1175/MWR-D-14-00416.1>.

- Potvin, C. K., E. M. Murillo, M. L. Flora, and D. M. Wheatley, 2017: Sensitivity of supercell simulations to initial-condition resolution. *J. Atmos. Sci.*, **74**, 5-26, <https://doi.org/10.1175/JAS-D-16-0098.1>.
- Rinehart, R. E., and E. T. Garvey, 1978: Three-dimensional storm motion detection by conventional weather radar. *Nature*, **273**, 287-289.
- Rotunno, R., and J. B. Klemp, 1985: On the rotation and propagation of numerically simulated supercell thunderstorms. *J. Atmos. Sci.*, **42**, 271-292, [https://doi.org/10.1175/1520-0469\(1985\)042<0271:OTRPO>2.0.CO;2](https://doi.org/10.1175/1520-0469(1985)042<0271:OTRPO>2.0.CO;2).
- Skamarock, W. C., and Coauthors, 2008: A description of the Advanced Research WRF version 3. NCAR Tech. Note NCAR/TN-475+STR, 113 pp., doi:10.5065/D68S4MVH.
- Smythe, G. R., and D. S. Znić, 1983: Correlation analysis of Doppler radar data and retrieval of the horizontal wind. *J. Climate and Appl. Meteorol.*, **22**, 297-311, [https://doi.org/10.1175/1520-0450\(1983\)022<0297:CAODRD>2.0.CO;2](https://doi.org/10.1175/1520-0450(1983)022<0297:CAODRD>2.0.CO;2).
- Thompson, G., R. M. Rasmussen, and K. Manning, 2004: Explicit forecasts of winter precipitation using an improved bulk microphysics scheme. Part I: Description and sensitivity analysis. *Mon. Wea. Rev.*, **132**, 519–542, [https://doi.org/10.1175/1520-0493\(2004\)132<0519:EFOWPU>2.0.CO;2](https://doi.org/10.1175/1520-0493(2004)132<0519:EFOWPU>2.0.CO;2).
- Thompson, G., P. R. Field, R. M. Rasmussen, and W. R. Hall, 2008: Explicit forecasts of winter precipitation using an improved bulk microphysics scheme. Part II: Implementation of a new snow parameterization. *Mon. Wea. Rev.*, **136**, 5095–5115, <https://doi.org/10.1175/2008MWR2387.1>.
- Trapp, R. J., and B. H. Fiedler, 1995: Tornado-like vortexgenesis in a simplified numerical model. *J. Atmos. Sci.*, **52**, 3757–3778, [https://doi.org/10.1175/1520-0469\(1995\)052<3757:TLVIAS>2.0.CO;2](https://doi.org/10.1175/1520-0469(1995)052<3757:TLVIAS>2.0.CO;2).
- Wicker, L. J., and R. B. Wilhelmson, 1995: Simulation and analysis of tornado development and decay within a three-dimensional supercell thunderstorm. *J. Atmos. Sci.*, **52**, 2675-2703, [https://doi.org/10.1175/1520-0469\(1995\)052<2675:SAOTD>2.0.CO;2](https://doi.org/10.1175/1520-0469(1995)052<2675:SAOTD>2.0.CO;2).
- Xu, Q., and L. Wei, 2013: Prognostic equation for radar radial velocity derived by considering atmospheric refraction and Earth curvature. *J. Atmos. Sci.*, **70**, 3328-3338, <https://doi.org/10.1175/JAS-D-13-011.1>.

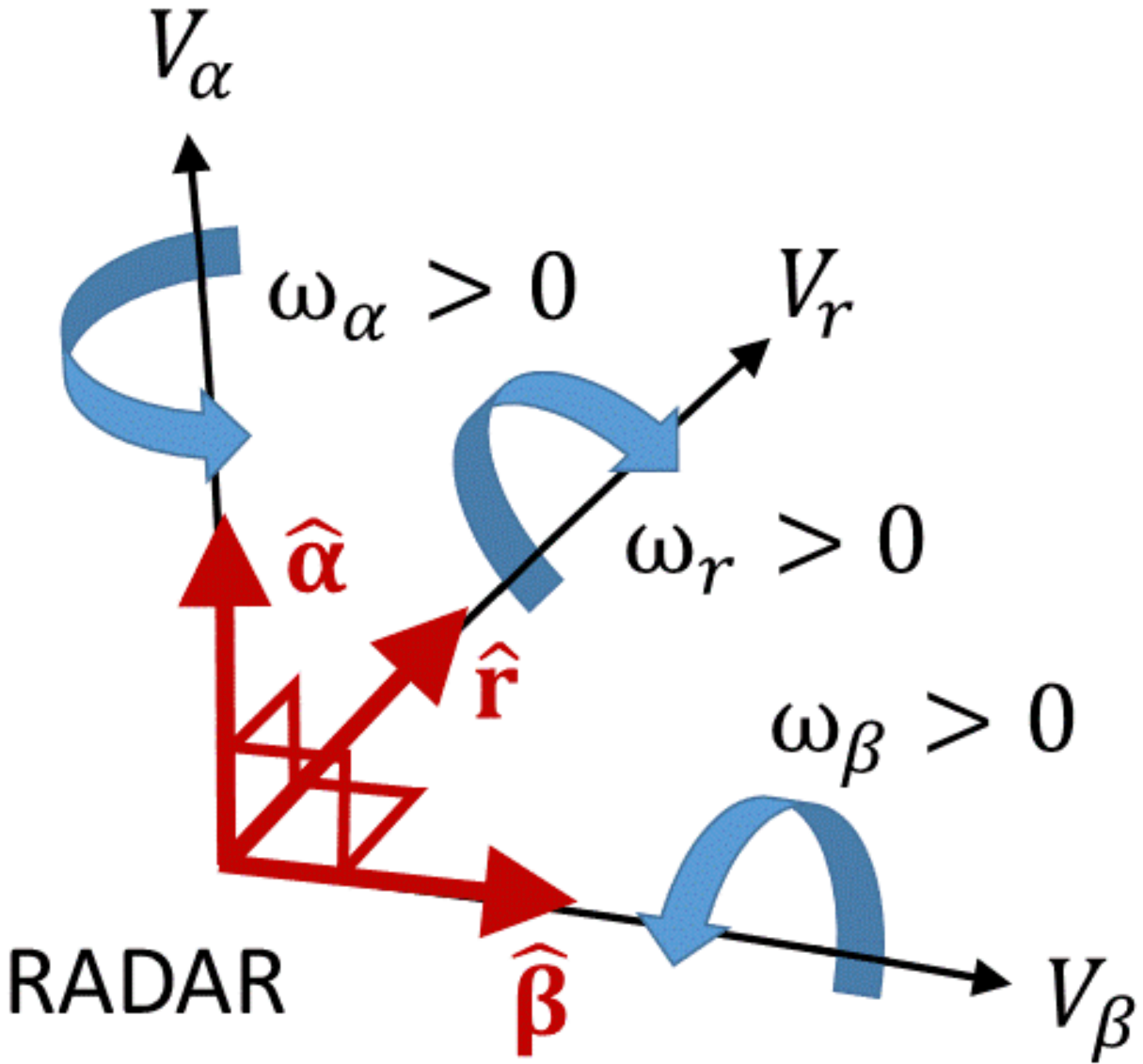


FIG. 1. Illustration of unit basis vectors (red) (\hat{r} , $\hat{\alpha}$, $\hat{\beta}$) of the curvilinear coordinate system and 3D velocity (V_r , V_α , V_β) and vorticity (ω_r , ω_α , ω_β) components as seen by the Doppler radar. Positive rotation is counterclockwise about the axis of rotation in each positive direction of \hat{r} , $\hat{\alpha}$, and $\hat{\beta}$. Blue curved arrow represents the sense of rotation about the axis of rotation from a 3-D perspective. Note that the axes are slightly curved, because the curvature is locally very small and the unit vectors are tangents.

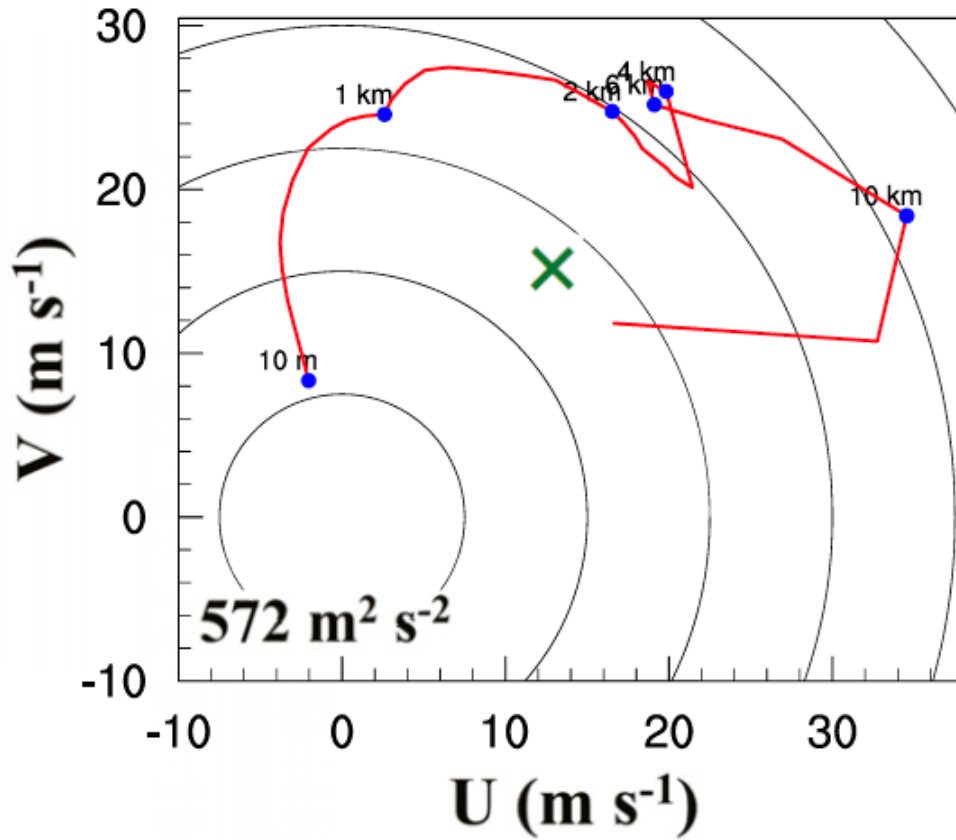


FIG. 2. Hodograph used in the El Reno simulation. The 0-3 km AGL storm-relative helicity (SRH, $\text{m}^2 \text{ s}^{-2}$) is indicated on the hodograph plot. Mean storm motion vector used in SRH calculations is indicated by green X on the hodograph. Blue dots represent heights above the model floor. These vectors were computed using the location of the hook echo signature at $t = 30$ and $t = 120$ min. (After Potvin and Flora 2015).

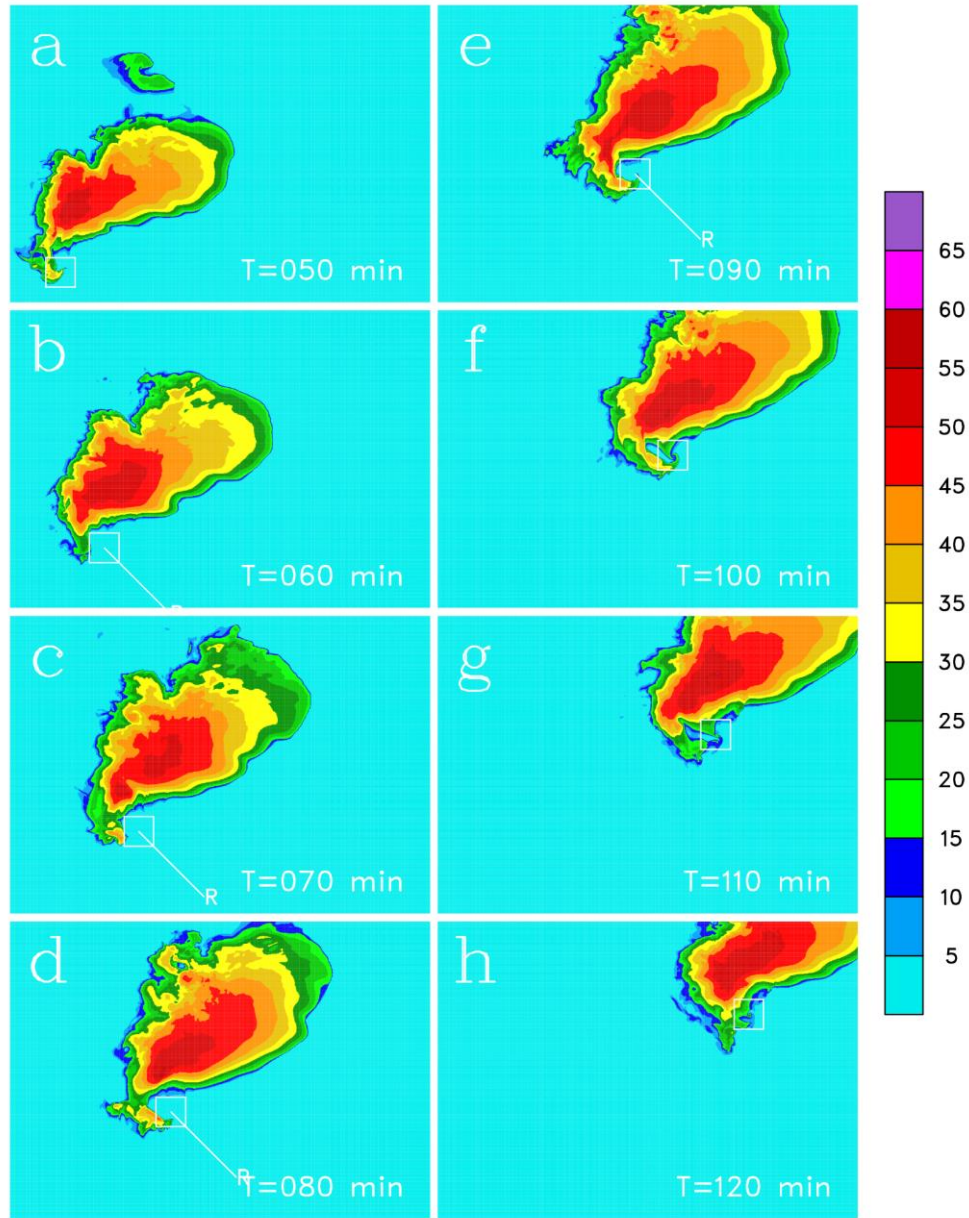


FIG. 3. Illustration of evolving low-level reflectivity fields at $t =$ (a) 50, (b) 60, (c) 70, (d) 80, (e) 90, (f) 100, (g) 110 and (h) 120 min into the simulations. The size of the large grid is approximately 114 km x 80 km; a small grid size of 8 x 8 km is indicated by a white smaller square. The center of the “translating” square is located at 25 km and 315° azimuth from the Doppler radar (R) and moves parallel to the storm motion vector. This square will be enlarged for examining the simulated signatures of Doppler velocity and reflectivity and also signatures of normal and azimuthal vorticity components. Vertical reflectivity scale (dBZ) is indicated on the right side.

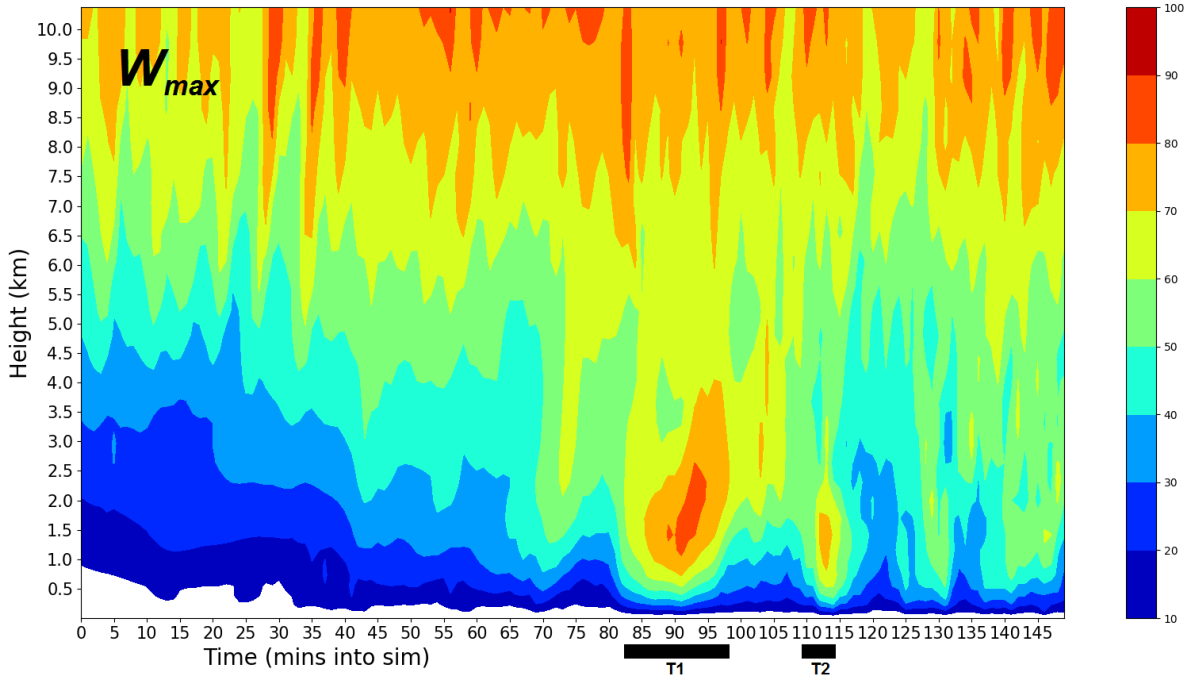


FIG. 4. Height-time plot of the numerical vertical velocity (W_{max} , m s^{-1}) peaks. Black rectangles represent durations of two simulated tornadoes, as indicated by T1 and T2. Near the ground, a white shading refers to $0 < w < 10 \text{ m s}^{-1}$.

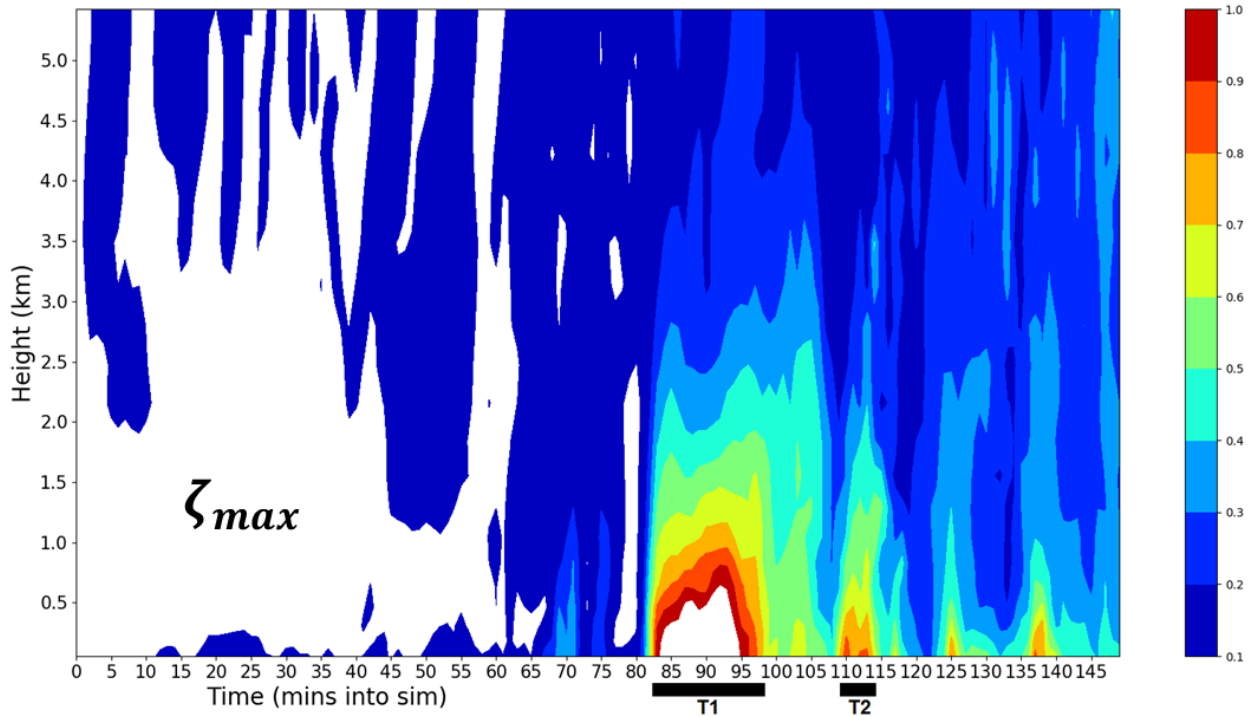


FIG. 5. Height-time plot of the numerical vertical vorticity (ζ_{max} , s^{-1}) peaks. White shading surrounded by dark red shading refers to $\zeta_{max} > 1.0 \text{ s}^{-1}$. The maximum value of ζ_{max} is 1.3 s^{-1} . The other white shading surrounded by a dark blue shading refers to $0 < \zeta_{max} < 0.1 \text{ s}^{-1}$. Black rectangles represent durations of two tornadoes, as indicated by T1 and T2.

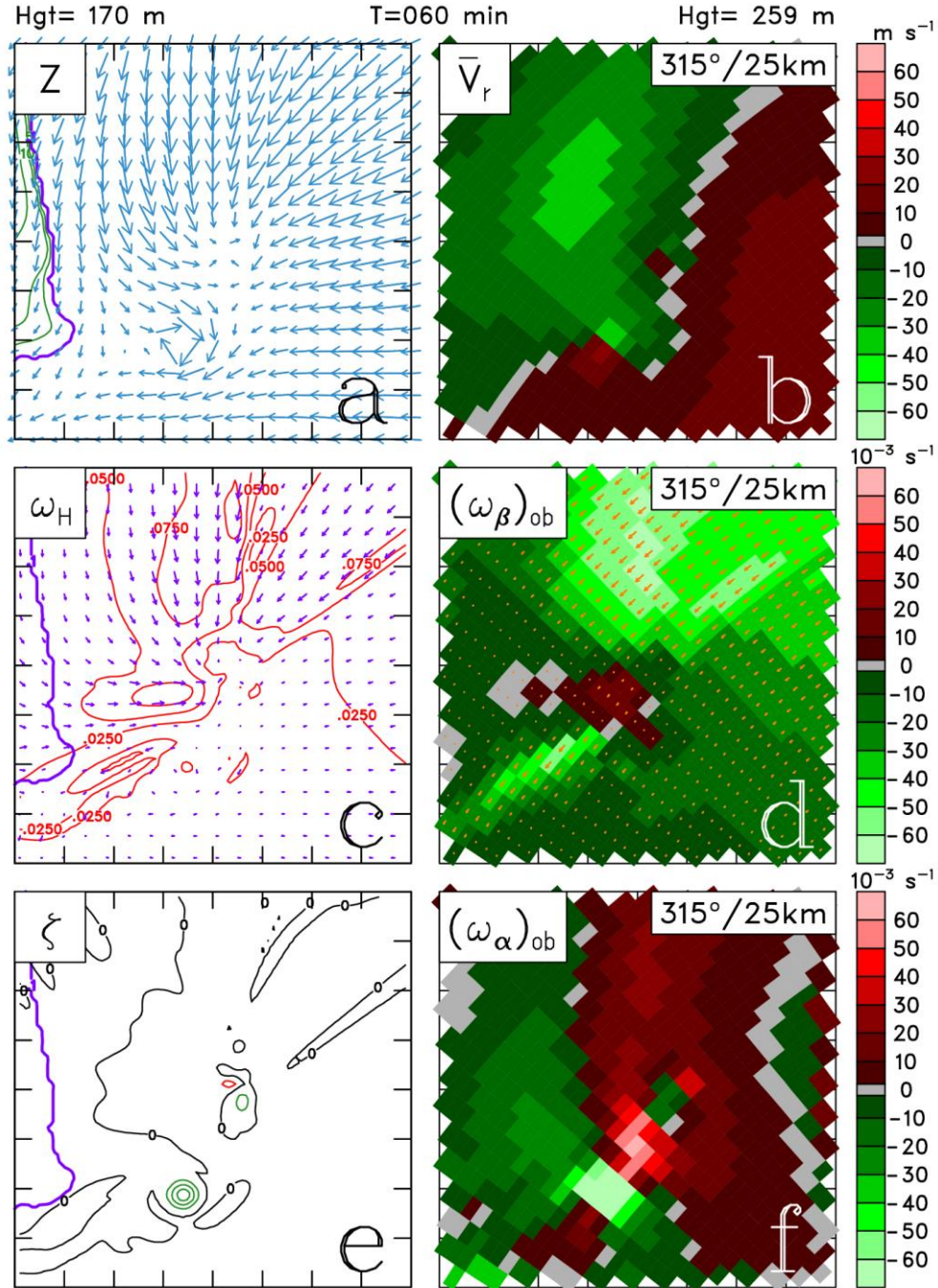


FIG. 6. Horizontal cross-sections valid at $t = 60$ min: (a) storm-relative, horizontal wind vectors (blue) with superimposed reflectivity (Z ; green dBZ contours > purple 0.1 dBZ contour), (b) simulated mean Doppler velocity component (\bar{V}_r ; m s^{-1}), (c) horizontal vorticity (purple) vectors ($\omega_H = \xi\mathbf{i} + \eta\mathbf{j}$; red contours, s^{-1}) with superimposed reflectivity (purple contour, 0.1 dBZ), (d) simulated Doppler azimuthal vorticity [$(\omega_\beta)_{ob}$; s^{-1}] with superimposed orange vectors being normal to radar viewing direction, (e) vertical vorticity (ζ ; red and green nonzero contours and black zero contours, s^{-1}) with superimposed reflectivity (purple contour, 0.1 dBZ), and (f) simulated Doppler normal vorticity [$(\omega_\alpha)_{ob}$; s^{-1}]. Grid size is $8 \text{ km} \times 8 \text{ km}$ with one tick mark equaling 1 km . In panels (a), (c) and (e), the center grid height is indicated at

the top, left corner and is approximately close to the center grid height at 25 km from the radar. In panels (b), (d) and (f), the virtual WSR-88D radar is assumed to be located to the southeast of the center grid so that the radar is pointing toward the grid center (25 km and 315° azimuth from the radar, indicated by the upper-right corner). The center grid height (m) of the radar at 25 km is indicated at the top, right corner of panel (b). Range spacing, azimuth interval, and elevation angle are 250 m, 1.0° and 0.5°, respectively. Vertical bar scales are indicated on the right-hand side.

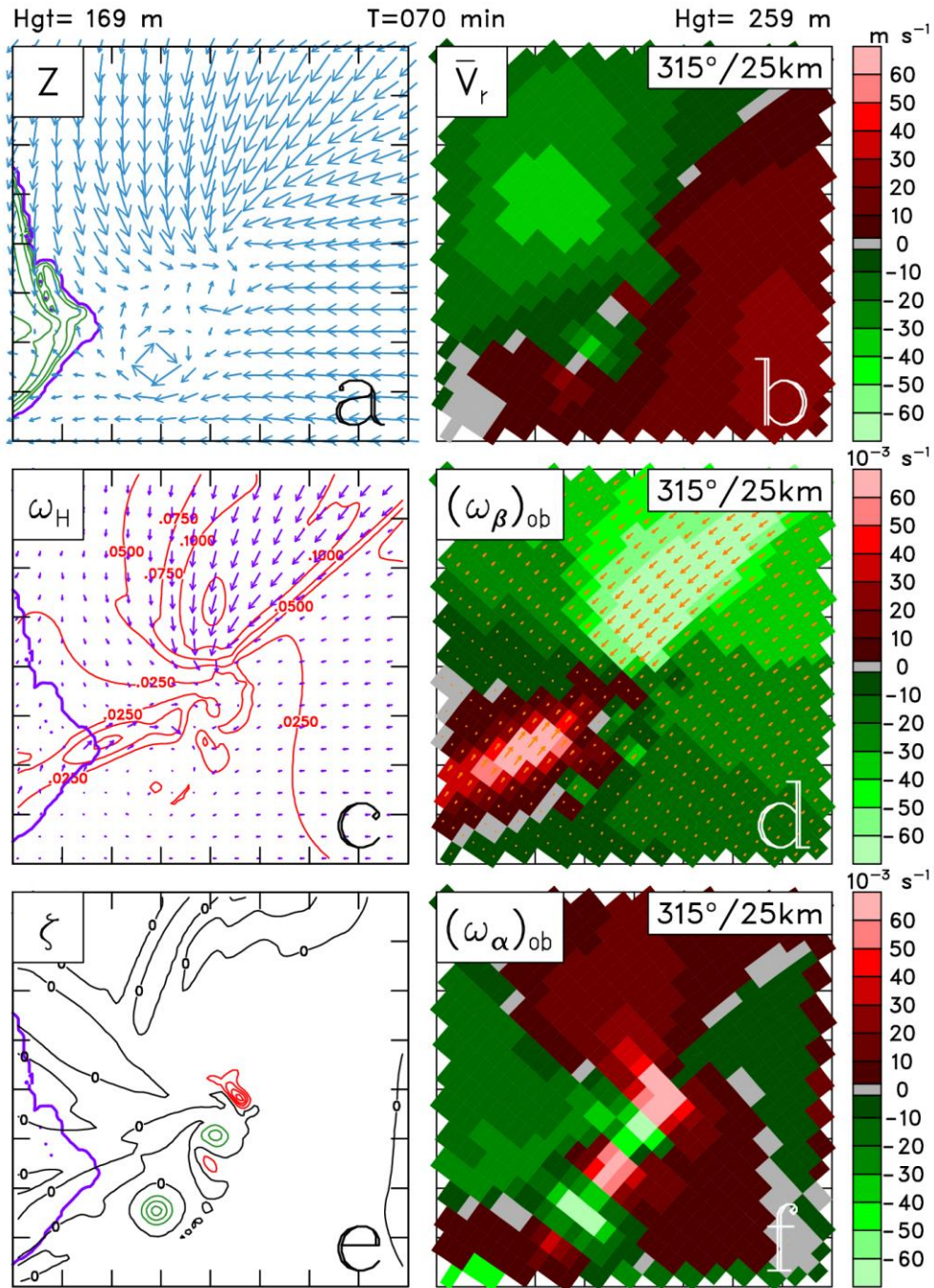


FIG. 7. Same as FIG. 6, except at $t = 70$ min.

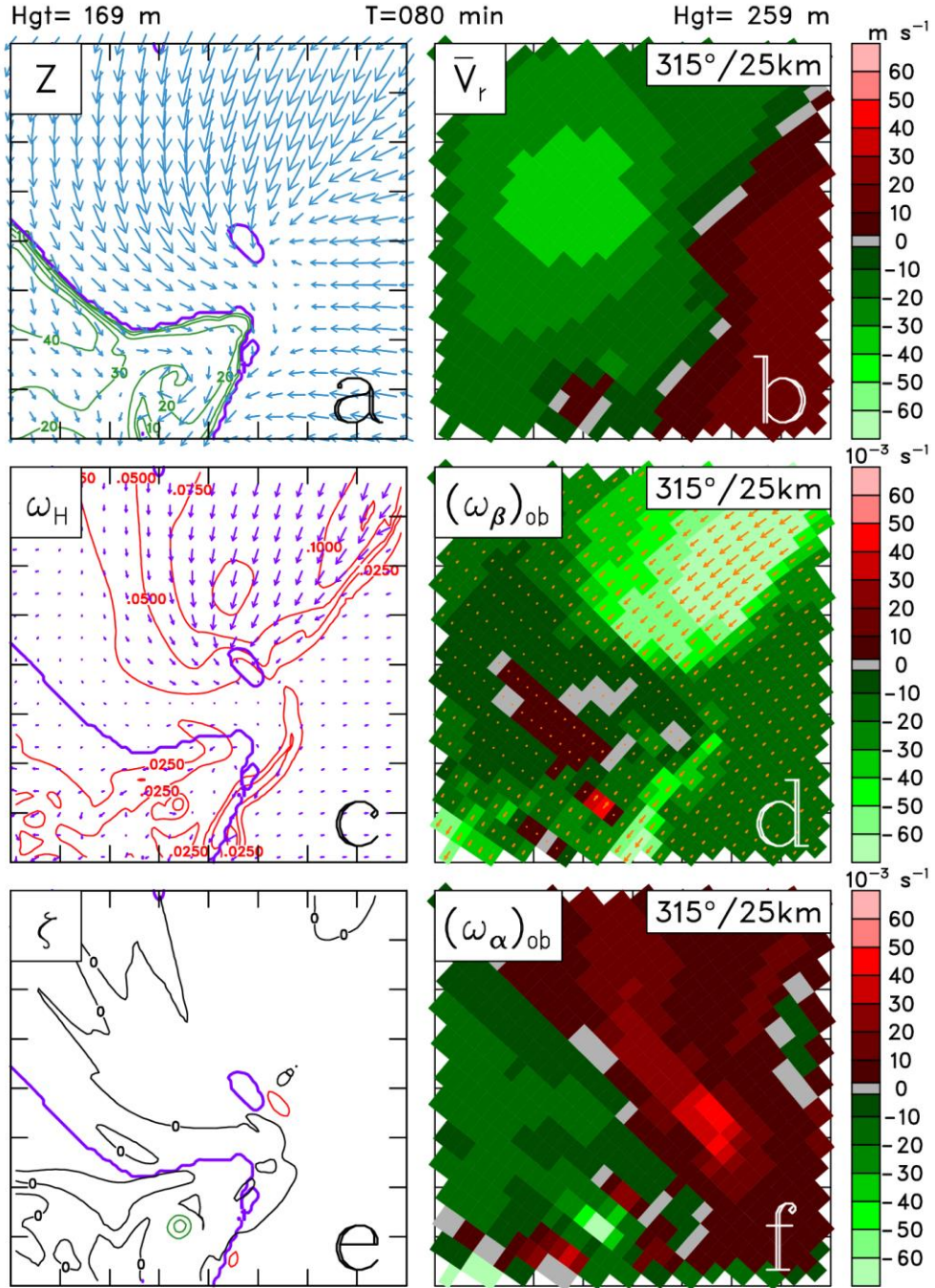


FIG. 8. Same as FIG. 6, except at $t = 80$ min.

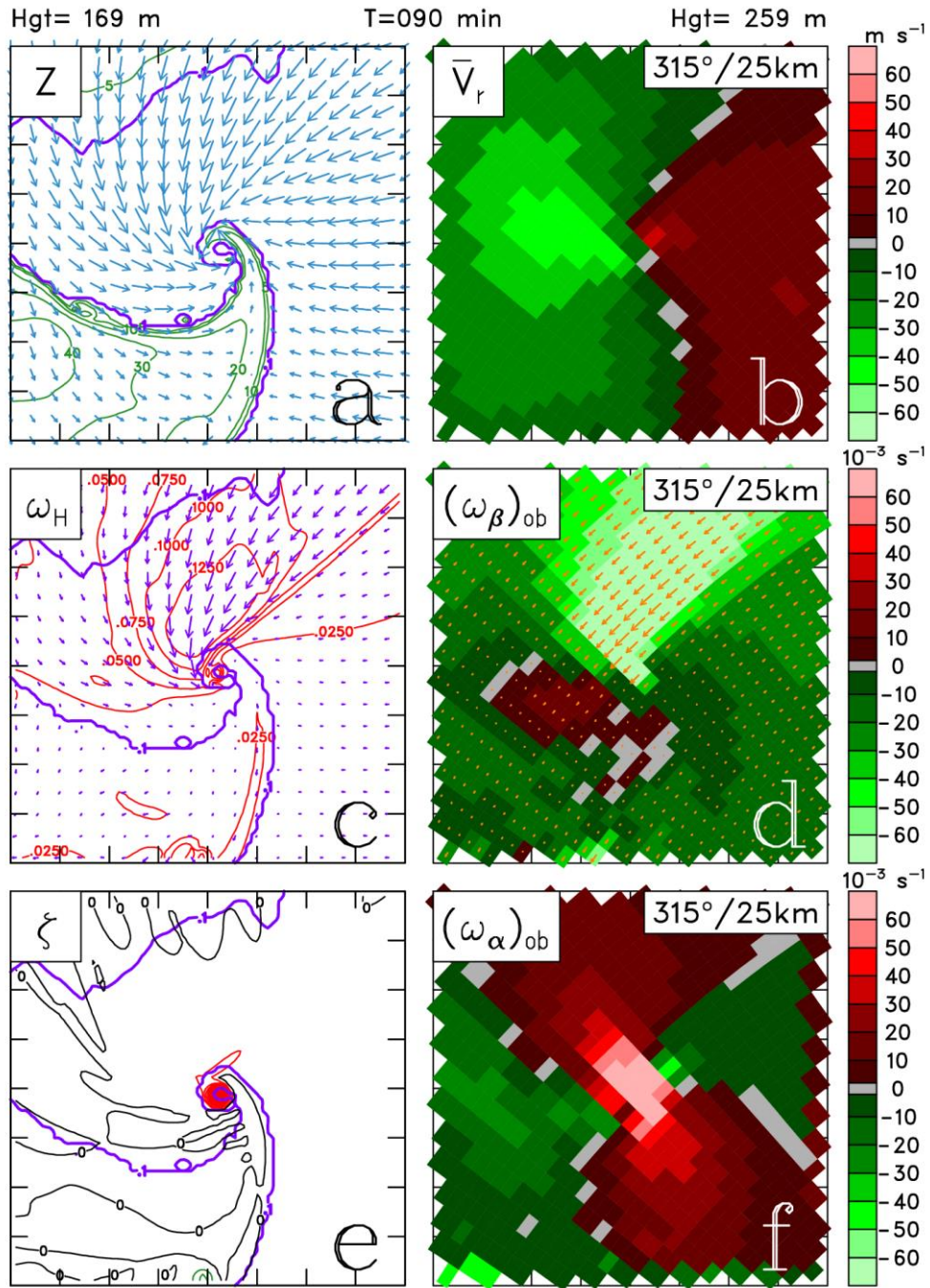


FIG. 9. Same as FIG. 6, except at $t = 90$ min.